Nano Research
2022, 15(5): 4739–4746

ISSN 1998-0124 CN 11-5974/O4
https://doi.org/10.1007/s12274-022-4117-9

High thermoelectric properties with low thermal conductivity due to the porous structure induced by the dendritic branching in n-type PbS

Zhenyu Zhu[1], Janak Tiwari[2], Tianli Feng[2], Zhan Shi[3], Yue Lou[1] (✉), and Biao Xu[1,4] (✉)

[1] *School of Chemistry and Chemical Engineering, Nanjing University of Science and Technology, Nanjing 210094, China*
[2] *Department of Mechanical Engineering, The University of Utah, Salt Lake City, UT 84112, USA*
[3] *State Key Laboratory of Inorganic Synthesis and Preparative Chemistry, College of Chemistry, Jilin University, Changchun 130012, China*
[4] *State Key Laboratory of Coordination Chemistry, School of Chemistry and Chemical Engineering, Nanjing University, Nanjing 210000, China*

Received: 15 December 2021 / **Revised:** 24 December 2021 / **Accepted:** 26 December 2021

ABSTRACT

PbS-based thermoelectric materials have attracted extensive attention in recent years for the advantages of earth abundancy and low cost, which is considered to be a substitute for traditional PbTe material. However, their high thermal conductivity restricts its development. Hence, in order to improve their thermoelectric performance from reducing the thermal conductivity, a kind of dendritic PbS with controlled crystal grain and morphology are obtained by solution synthesis. By adjusting the amount of surfactant (CTAB), the specific formation process of dendrites is regulated. After sintering, the dendritic PbS nanoparticles are easy to form porous structure due to the overlapping and staggered arrangement of dendritic branches. For comparison, we also prepare a kind of regular octahedral PbS and a dense packing arrangement is formed because of the integrity of the octahedral structure. DFT-based Boltzmann transport equation is used to prove the crucial role of porous structure in scattering phonon. Finally, a maximum zT = 1.0 at 773 K in n-type PbS is obtained, which still keep a high-speed growth and is expected to get higher zT value in a higher temperature region. Our work may shed light to other thermoelectric materials from the formation of porous structure to reduce the thermal conductivity.

KEYWORDS

thermoelectric materials, lead sulfide, solution synthesis, porous structure.

1 Instruction

Thermoelectric (TE) devices can realize the mutual conversion of heat energy and electric energy, which has become a hot research field in recent years because they are miniaturized, portable and noiseless [1–3]. However, the relatively low conversion efficiency of thermoelectric materials limits their large-scale practical application [4]. Generally, the performance of thermoelectric material is determined by a dimensionless figure of merit (zT), which can be defined as $S^2\sigma T/(\kappa_{\mathrm{lat}}+\kappa_{\mathrm{ele}})$, where σ is the electrical conductivity, S denotes Seebeck coefficient, T is the working temperature in Kelvin, κ_{lat} is the lattice thermal conductivity and κ_{ele} is the electronic thermal conductivity, respectively. Therefore, most of the current experimental studies are aimed at improving the zT value of TE materials in order to improve their conversion efficiency and provide references for practical industrial applications. Meanwhile, improving portability of devices also plays a significant role, but remains largely underexplored. Toward this target, synthesizing nanocrystals with irregular shape such as hollow [5], concave [6] and branched nanostructures morphologies as precursors to realize imperfect stacking of building blocks is an effective method. On the one hand, the introduction of nanoporosity can lower the thermal conductivity of the final bulk matrix. On the other hand, controlling porous nanostructure also plays the dominant role in lowering mass density to improve portability of devices [7, 8].

PbS thermoelectric materials are a traditional thermoelectric material with cubic rock-salt structure, which have the advantages of abundant sources and low price [9]. However, compared with PbTe, their relatively high thermal conductivity restricts their further applications. Hence, finding an efficient way to optimize thermal transport of PbS is the key parameter to enhance their zT. So far, various methods to reduce the thermal conductivity have been reported. For examples, Zhao et al. reported that PbS-based samples with selected second phases such as Bi_2S_3 [10], CaS [11] and ZnS [12] can reduce the thermal conductivity. Yang et al. reported that multiscale structure just like point defect and grain boundary can realize the reduction of thermal conductivity through enhancing interfacial scattering [13]. Solid solution method had also been tried to reduce the lattice thermal conductivity by introducing different scattering mechanism, like PbSe-PbS [14, 15] and PbTe-PbS [16, 17]. However, because the commonly used top-down synthesis method such as melt spinning or mechanical alloying cannot realize controllable synthesis of nanoparticles with specific morphology, reducing the lattice thermal conductivity of PbS nanoparticles by improving the porous structure of building blocks is difficult. By contrast,

---

Address correspondence to Yue Lou, wuxiaoshuai365@163.com; Biao Xu, xubiao@njust.edu.cn

solution synthesis, as a bottom-up synthesis strategy [18, 19], becomes a superior alternative due to its incomparable advantages in precisely controlling nanoparticle size, shape and surface chemistry [20–22]. Therefore, introduction of porous structure is an effective tool to solve the above problem, which not only can optimize the performance of thermoelectric materials by scattering phonon through three-dimensional self-assembly porous structure but can also improve their portability.

In this work, a kind of dendritic PbS is designed and synthesized by hydrothermal method. The dendritic branching structure can be effectively controlled by adjusting the amount of CTAB. As a comparison, octahedral PbS are prepared by flask synthesis method. Relative density of bulk monolith built by dendritic PbS reaches 92% of the arrangement of dense accumulation of octahedral PbS under the same consolidation condition. Moreover, the porous structure caused by the branching morphology has a significant effect on reducing the thermal conductivity of PbS materials. Eventually, the thermal conductivity of dendritic PbS decreases by 30% at 773K with no deteriorated electrical conductivity and the final zT value increases by 230% compared with octahedral PbS. Theoretical simulation proved that construction of porous structure has a positive influence on enhancing phonon scattering, resulting in the reduction of lattice thermal conductivity. As expected, the maximum zT value of dendritic PbS reaches 1.0 at 773 K, which is nearly 50% higher than that of the pristine PbS.

2 Experimental

2.1 Synthesis

Chemicals: lead acetate trihydrate ($Pb(CH_3COO)_2{\cdot}3H_2O$, 99.99%), thiourea ($CH_4N_2S$, 99%) and cetyl trimethyl ammonium bromide (CTAB, 99%) were purchased from Shanghai Aladdin Biochemical Technology Co., Ltd. Acetic acid (CH_3COOH, 99%) and thioacetamide (CH_3CSNH_2, 99%) were purchased from Shanghai Macklin Biochemical Technology Co., Ltd. All chemicals were used as received without further purification.

Synthesis of dendritic PbS nanocrystals: 5 mmol of $Pb(CH_3COO)_2{\cdot}3H_2O$ (1.8964 g), 15 mmol of thiourea (1.1418 g) and CTAB (= 0, 0.1, 0.3 and 0.5 g, respectively) were successively dissolved into 60 mL deionized water under magnetic stirring for 10 min. Then, the solution was transferred to an autoclave made of stainless steel lined with Teflon. After that, the autoclave was tightly sealed and kept at 120 °C for 24 h. After the reaction was completed, the black products were isolated by centrifugation at 12,000 rpm for 1 min and washed with absolute ethanol and deionized water for several times. Finally, the products were vacuum dried in a 60 °C oven for 6 h.

Synthesis of octahedral PbS nanocrystals: 6.82 mmol of $Pb(CH_3COO)_2{\cdot}3H_2O$ (1.8964 g), 6.82 mmol of thioacetamide (0.5124 g), 12.12 mmol of acetic acid (1.6214 g) and CTAB (0.6217 g) were weighed and then dissolved into 300 mL of deionized water. This solution was kept at 80 °C under magnetic stirring and heated for 24 h. The washing procedure was the same as above.

2.2 Spark plasma sintering (SPS) and thermoelectric measurements

The sample powders were compacted into pellets (10 mm diameter, 2 mm thickness) in a graphite die using a spark plasma sintering system (LABOX-110, Sinter Land). The samples were held at an axial pressure of 20 MPa and a temperature of 873 K for 5 min, then the pressure was quickly released and the pellet was peeled off. Seebeck coefficient and electrical resistivity were obtained simultaneously in an LSR-3 LINSEIS system in the range from 323 to 773 K under helium atmosphere. The total thermal conductivity (κ) was calculated by the formula, $\kappa = D{\cdot}C_p{\cdot}\rho$, where the thermal diffusion coefficient (D) was measured under same temperature range with a Netzsch LFA457 equipment, the specific heat capacity (C_p) was estimated using the method of Dulong-Petit law with a value of 0.2085 $J{\cdot}g^{-1}{\cdot}K^{-1}$ and the mass density (ρ) was measured by the Archimedes' method. The relative density was calculated by ρ/ρ_0, where ρ_0 is single-crystal density of PbS and the value is 7.5 $g{\cdot}cm^{-3}$. The porosity was calculated by $(1-\rho/\rho_0)$.

2.3 Characterization

X-ray diffraction (XRD) was conducted in a Bruker D8 Advance diffractometer, with Cu Kα radiation (λ = 1.5418 Å), at 40 kV and 40 mA. The morphology of nanoparticles was observed by transmission electron microscope (TEM, FEI TECNAI G2 20 LaB6) and scanning electron microscope (SEM, JSM-IT500HR). We also carried out energy dispersive X-ray spectroscopy (EDS, JEOL JSM-6700F) to obtain elemental profiles. Thermal gravimetric analysis (TGA) of the as-synthesized powders were carried out on a TGA/SDTA851E thermal analyzer from room temperature to 600 °C with a heating rate of 10 $°C{\cdot}min^{-1}$ in N_2. Hall coefficients (R_H) were measured under a reversible magnetic field (1.5 T) by the Van der Pauw method.

3 Result and discussion

The samples of dendrite PbS were prepared by facile hydrothermal method with different amount of CTAB, in which the PbS materials with the addition of 0 g CTAB, 0.1 g CTAB, 0.3 g CTAB and 0.5 g CTAB are denoted as 1#, 2#, 3# and 4# respectively. The contrastive octahedral PbS sample synthesized by a flask method is denoted as 5#. **Figure 1(a)** shows the XRD patterns of dendritic PbS and octahedral PbS, the peak positions at 25.9°, 30.0°, 43.0°, 50.9°, 53.4°, 62.5°, and 68.9° correspond to the (111), (200), (220), (311), (222), (400), and (331) crystal planes respectively, which are all in accordance with the standard diffraction pattern (PDF65-2935), indicating that these samples are of pure phase. Compared with pristine PbS (1#), the intensity of (200) of dendritic sample is increased, even higher than that of (111), indicating that the surfactant, CTAB, plays a key role in controlling the growth orientation of crystal in solution synthesis [23].

Several techniques like SEM, TEM, high-resolution TEM (HRTEM) and EDS mapping were performed to reveal the size, morphology and composition of the as-synthesized dendrite PbS (4#) powder. **Figure 1(b)** is a typical TEM image of the product, which clearly shows a dendrite structure. Each individual dendrite PbS has a three-dimensional (3D) structure with one trunk and several branches. **Figure 1(c)** shows that the lattice fringe spacing is measured as 0.341 nm which can be indexed to the (111) lattice plane of dendrite PbS (4#), implying that the trunk of dendrite PbS grow along the [111] crystal direction. **Figure 1(d)** shows that the fringe spacing of the branch of dendrite PbS is determined to be 0.296 nm, which is close to the (200) lattice spacing of the bulk PbS, indicating that the crystal growth of the branch is preferential in the [100] direction. Beside the complete lattice stripes, an array of distortions can be seen in dendrite PbS from Fig. 1(d). These lattice defects caused during synthesis process can enhance phonon scattering and will play an important role in reducing thermal conductivity. EDS mapping images (Fig. 1(e)) demonstrate that in addition to the Pb and S elements, Br element derived from the surfactant (CTAB) also uniformly distribute in the samples. This illustrates Br element participated in the reaction process and was retained in the samples.

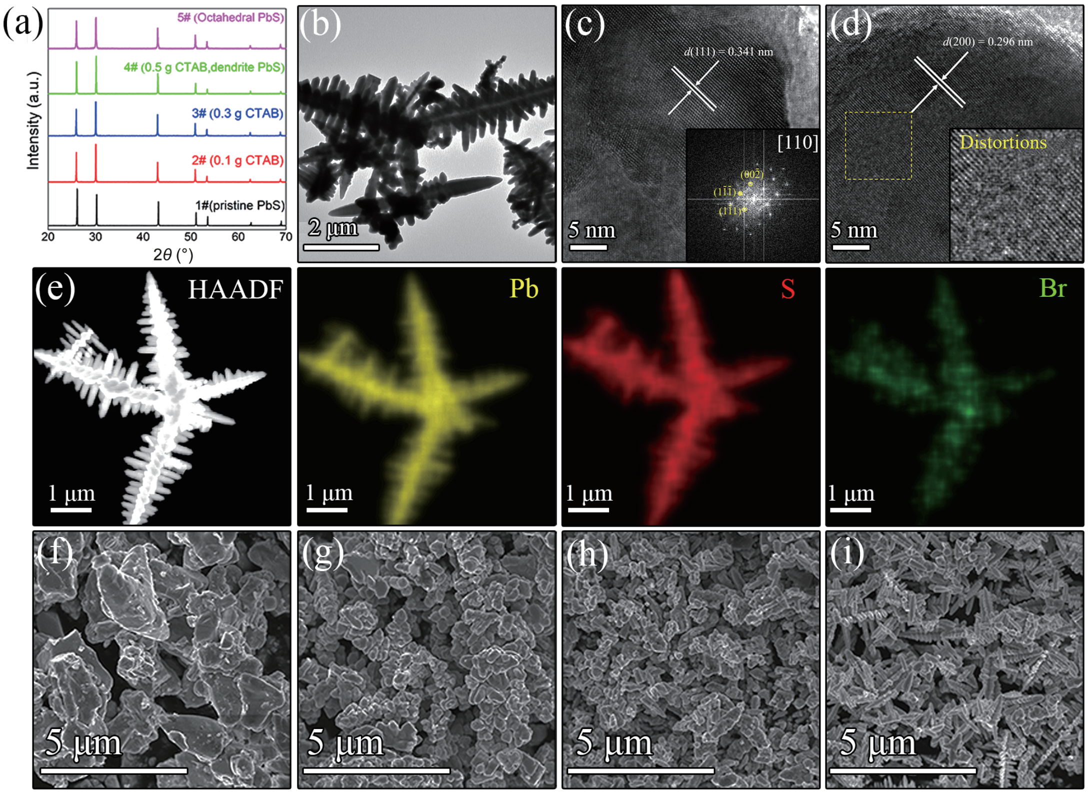

Figure 1 (a) The XRD patterns of samples 1#, 2#, 3#, 4# and 5# respectively. (b) The low-magnification TEM of the dendrite PbS (4#), which shows a dendritic staggered arrangement structure. (c) The high-magnification TEM recorded from the trunk of the dendrite PbS of b. (d) HRTEM image recorded from the branch of dendrite PbS of (b). (e) The EDS mapping images of dendrite PbS sample (4#). (f)–(i) SEM images of dendrite PbS synthesized with 0 g (1#), 0.1 g (2#), 0.3 g (3#) and 0.5 g CTAB (4#), respectively.

As shown in Figs. 1(f)–1(i), the SEM images of dendrite PbS synthesized with 0 g (1#), 0.1 g (2#), 0.3 g (3#) and 0.5 g CTAB (4#) were performed to reveal the mechanism of the growth process of dendrites. The surfactant of CTAB was used to regulate morphology and control the length of dendritic branches. As has been reported in many literatures [24], CTAB can adsorb onto the surface of the small nuclei of crystal and influence crystal growth orientation. The pristine PbS (1#) without CTAB is irregularly shaped with the size of 4–5 μm. With the addition of CTAB, the morphology of PbS has changed and the structure of dendrite PbS is becoming more and obvious. Firstly, the trunk structure grows and subsequently the nanorods of branching structure grows perpendicular to the trunk. In the evolution process from 1# to 4#, we can effectively see the difference of its branching structure. The sample synthesized with 0.1 g CTAB (2#) has the shortest length of branches. When the amount of CTAB increases to 0.3 g (3#), the branches are more obvious as compared with the 2#. Figure 1(d) shows that the dendritic branch structure of 4# are perfectly formed with its length of branches ranging from 100–600 nm.

In addition, the contrastive octahedral PbS sample was also characterized by several techniques like HRTEM, Fast Fourier transform (FFT) and EDS. According to SEM and TEM images (Figs. 2(a) and 2(b)), the as-synthesized crystals were approximate octahedral shape with a mean diameter of 150 nm. As shown in Fig. 2(c), HRTEM image of a representative PbS nanocrystal confirms the high crystallinity of the as-synthesized nanocrystals without detectable structural defects like dislocations and distortions. And the fringe spacing of octahedral PbS is 0.341 nm, corresponding to the lattice planes of (111), which agrees with the crystal orientation of octahedral morphology. The elemental mapping images of Pb, S, and Br elements using EDS analyzer are shown in Fig. 2(d), which identifies the presence of Pb, S, Br. The elements of Pb, S, and Br are uniformly distributed in the octahedral PbS. The EDS energy spectrum of octahedral PbS (Fig. S1(e) in the Electronic Supplementary Material (ESM)) shows a tiny proportion of 1 atom% Br which is corresponding with the doping amount of dendrite PbS (4#) sample and the doping amount of 1#, 2# and 3# was 0%, 0.29%, 0.71%, respectively.

To explore thermoelectric performance of our PbS samples, those samples were sintered by spark plasma sintering (SPS). The crystal structure of all samples remained unchanged after sintering, and the XRD pattern of the sintered samples can be seen in Fig. S3 in the ESM. As shown in Table 1, obvious differences in the relative density are found among samples with different morphologies. As we anticipated, the branching of dendritic structure is the key factor for the introduction of porous structure. While the branch structure become clearer from 1# to 4#, the volume of pore of bulk matrix gradually increased which led to monotonously reduced relative densities of PbS bulk matrix. The SEM of fractography of bulk matrix (1#, 2#, 3#) are shown in the Fig. S2 in the ESM. The monolith sintered from 1#, 2# and 3# have finer grains, fewer pores and higher density. Due to the random distribution of dendrites and the staggered arrangement of branching structures in the sintering process, dendrite PbS (4#) tends to form porous structure, resulting in the lowest relative density of 92% and the highest porosity of 8%. In addition, Figs. 3(a) and 3(b) show the SEM morphology of the fractured surfaces of dendrite PbS matrix (4#) and octahedral PbS matrix (5#), from which the difference in porosity can be clearly seen. In the sintered dendrites samples, the porous structure is obvious and the distribution is uniform, which indicates that the shape-controlled nanoparticles synthesized by solution is a key factor of the formation of bulk matrix with porous structure. In contrast, octahedral PbS is easy to form a dense packing mode owing to its highly regular shape. A higher propensity of grain growth occurred during the sintering process, which results in the formation of large bulk structure with 6–7 μm grain size and the high relative density.

In order to explore the effect of porous structure on the

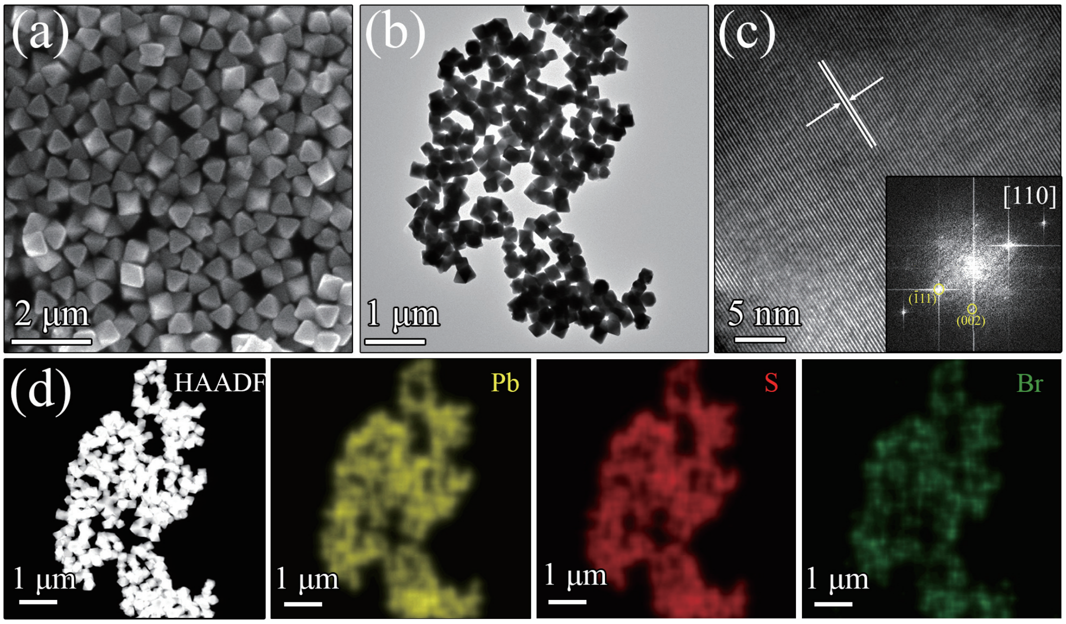

Figure 2 (a) The SEM image of the octahedral PbS. (b) and (c) The low-magnification and high-magnification TEM of the octahedral PbS (5#), the inset shows corresponding FFT pattern. (d) The EDS mapping images of octahedral PbS (sample 5#).

Table 1 Comparison of relative density, porosity, carrier concentration n_H, and carrier mobility μ_H at 323 K for all samples

Sample name	Relative density	Porosity	n_H (cm^{-3})	μ_H (cm^2·V^{-1}·s^{-1})
1#	99.6%	0.4%	7.6×10^{18}	101.4
2#	98.3%	1.7%	5.7×10^{19}	46
3#	96.4%	3.6%	7.0×10^{19}	56
4#	92.3%	7.7%	8.0×10^{19}	22
5#	98.1%	1.9%	8.1×10^{19}	19

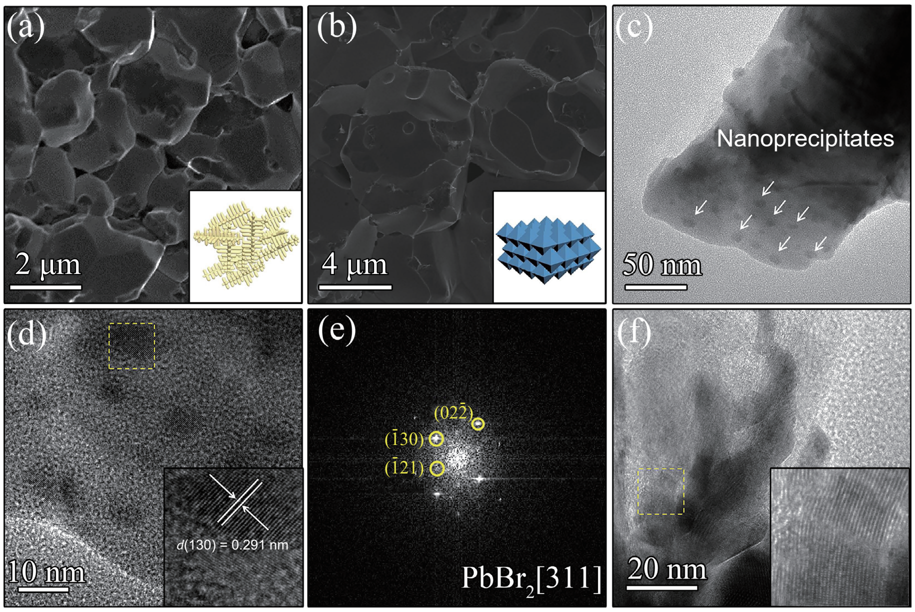

Figure 3 (a) and (b) SEM images of fractured surfaces of bulk matrix 4# (from dendrite PbS) and 5# (from octahedral PbS) sample with schematic illustrations of the possible packing inside. (c) TEM images of the sintered dendrite PbS sample shows some dark contrast. (d) HRTEM image depicting the lattice fringes of nanoprecipitates corresponding to PbBr$_2$. (e) FFT pattern of the nanoprecipitates, which shows the corresponding diffraction patterns of PbBr$_2$ along the [311] zone axis. (f) The lattice distortion caused by overlapping and interlacing stacking structure of the dendritic branches.

thermoelectric performance, we first tested their electrical properties in the temperature range from 323 to 773 K. In this temperature range, the monolith structure remains stable, the thermogravimetric analysis in this temperature interval is shown in Fig. S4 in the ESM. As shown in Fig. 4(a), all samples show a negative sign of Seebeck coefficients (S) that can be attributed to Br-doping, indicating all samples are n-type semiconductors and the major carriers are electrons. It is easily found that the absolute Seebeck coefficient (S) of all samples increases monotonously as temperature ascends. This characteristic trend implies a behavior of a degenerate semiconductor [10]. The Seebeck coefficient (S) of pristine PbS (1#) changes range from −196 to −340 μV·K^{-1} and the

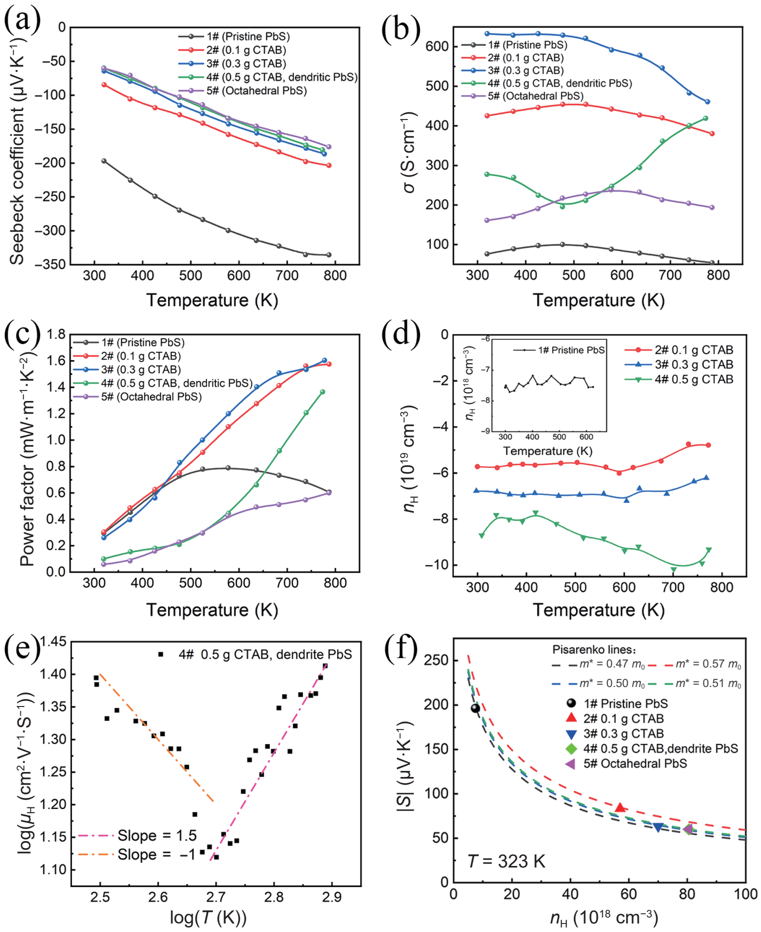

Figure 4 Temperature dependence of: (a) Seebeck coefficient S. (b) Electrical conductivity σ. (c) Power factor PF. (d) Carrier concentration n_H. (e) Carrier mobility μ_H. (f) Pisarenko plots.

S of other samples slight changes between −50 and −200 μV·K⁻¹. Apart from this, Seebeck coefficient also decreased slightly when the samples change from 1# to 4#, indicating the increase of carrier concentration caused by the increase of Br doping. This is also confirmed by the Hall test results, where the carrier concentration gradually increases as the sample changes from 1#–4# (Fig. 4(d)). The Pisarenko plots of a function of Seebeck coefficients and carrier concentration at 323 K are shown in Fig. 4(f), data points of experimental Seebeck coefficients distribute above the Pisarenko line with an effective charge carrier mass $m^* = 0.5m_o$, indicating that a parabolic band and an acoustic phonon scattering mechanism matches the experimental values very well. The increase of CTAB effectively increases the amount of doping of Br atoms and carrier concentration.

The electrical conductivity (σ) is plotted in Fig. 4(b). For the pristine PbS sample (1#), the σ increase first and then decrease with increasing temperature. The electrical conductivity (σ) of CTAB-added samples is obviously improved in the temperature range of 323–773 K and the 3# sample exhibits the highest conductivity, reaching 630 S·cm⁻¹ at 323 K and 460 S·cm⁻¹ at 773 K. Compared to the 2# sample, the highest conductivity can be attributed to the increased carrier concentration which greatly optimizes the electrical transport process. Actually, the electrical conductivity (σ) was calculated by $\sigma = n_H e \mu_H$, n_H is carrier concentration and μ_H is carrier mobility, where μ_H not only reflects the internal mobility of electrons, but also is a temperature-dependent parameter that reflects the effect of the scattering mechanism on the relaxation time at different temperature bands, roughly following the power law ($\mu_H \propto T^d$), when $d = -1.5$ denote the electron-phonon scattering and $d = 1.5$ denote electron-ionized impurity scattering [25, 26]. Figure 4(e) shows the corresponding T-dependent carrier mobility μ_H, in the low temperature region, the μ_H is decreased and follows the trend of $\mu_H \propto T^{-1}$, suggesting that the electron–phonon dominate the scattering mechanism [27] and also still mixes with electron–ionized impurity scattering, as will be confirmed below. At high temperature, μ_H increases roughly following $\mu_H \propto T^{1.5}$, but this does not mean that impurity scattering dominates this region, the main effect of impurity scattering goes to the low temperature region [28, 29], which means that there may be other scattering mechanisms, possibly the effect of nanopore scattering. μ_H for the other samples are shown in Fig. S5 in the ESM which do not show similar trends. As the result of the porous structure, 4# sample exhibits a relatively low electrical conductivity owing to the impaired μ_H, which lead to an obstruction of electrical transport process. At the same time, we propose that low σ of 5# sample can be ascribed to the difference of carrier mobility along different crystal directions since the high symmetry integrity of octahedral samples all grow along the [111] crystal plane.

The power factor (PF) which is calculated by $S^2\sigma$ can be seen from Fig. 4(c). Samples of 2# and 3# have the highest PF in view of the Seebeck coefficient (S) and high electrical conductivity (σ) which are greater than 1.5 mV·m⁻¹·K⁻² at 773 K, while 4# sample exhibits a PF of 1.36 mV·m⁻¹·K⁻² at 773 K due to the low σ.

Figure 5(a) displays the temperature-dependent κ of all samples (1#–5#) for comparison. Thermal conductivity decreases gradually from low temperature to high temperature because of the enhanced lattice vibration scattering [30, 31]. The increased carrier concentration caused by dopant will lead to an increase in electrical conductivity (σ) and carrier thermal conductivity (κ_{ele}). Hence, the pristine PbS sample (1#) shows the lowest thermal conductivity compared with other samples, which is similar to the

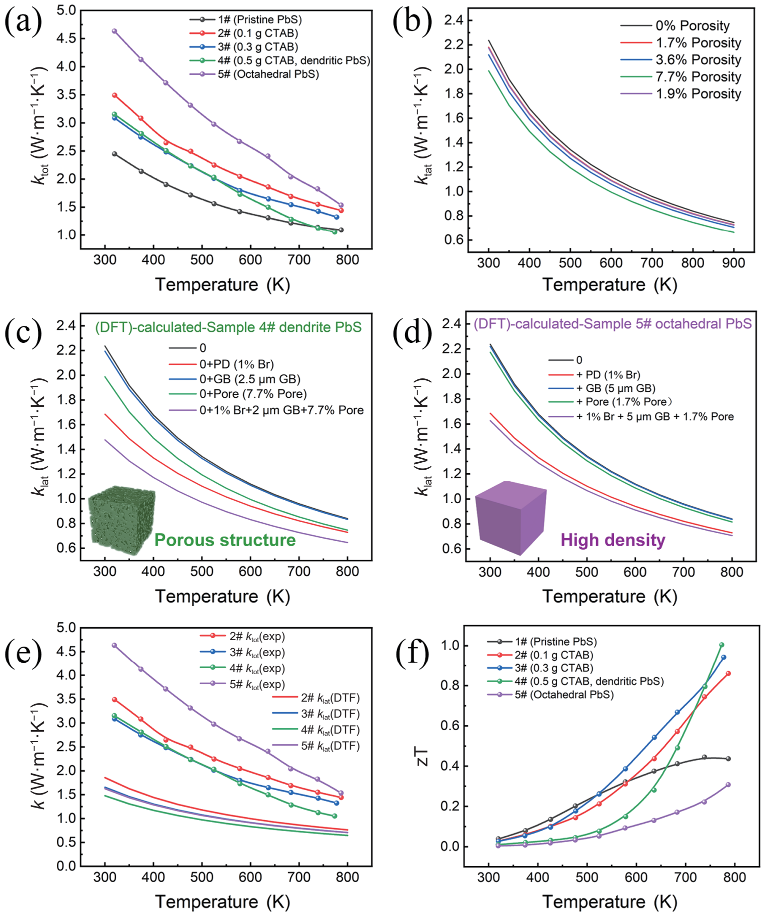

Figure 5 (a) Temperature dependence of κ_{tot} of all samples (1#–5#). (b) DFT-calculated contribution of different porosity to lattice thermal conductivity. (c) DFT-calculated κ_{lat} of 4# by considering the phonon scattering mechanisms of PD, GB and Pore. (d) DFT calculated κ_{lat} of 5# octahedron sample by considering the phonon scattering mechanisms of PD, GB and Pore. (e) The calculated lattice thermal conductivities (κ_{lat}) of these samples are compared to the experimentally measured data. (f) Temperature dependent of zT of all samples (1#–5#).

previous reports [13, 32, 33]. Moreover, it is found that with the obvious of dendritic branching structure, the relative density decreases and the porosity increases (2#–4#), which is significant in reducing thermal conductivity. At room temperature, the κ decreased from 3.45 W·m^{-1}·K^{-1} for the 2# sample to 3.18 W·m^{-1}·K^{-1} for the 4# sample. κ decreased from 1.45 W·m^{-1}·K^{-1} for the 2# sample to 1.05 W·m^{-1}·K^{-1} at 773 K for the 4# sample, representing a decrease of about 10% at room temperature and about 30% at 773 K.

In order to clearly reveal the effect of porous structure, a single variable on the lattice thermal conductivity by maintaining other effect factors constant was analyzed based on first principles density functional theory (DFT)-based phonon Boltzmann transport equation (BTE).

$$\frac{1}{\tau_{\mathrm{ph}}(q,j)}=\frac{1}{\tau_{\mathrm{anh}}(q,j)}+\frac{1}{\tau_{\mathrm{iso}}(q,j)}+\frac{1}{\tau_{\mathrm{def}}(q,j)}+\frac{1}{\tau_{\mathrm{gb}}(q,j)}+\frac{1}{\tau_{\mathrm{pore}}(q,j)} \quad (1)$$

We are using the relaxation time approximation by treating lattice thermal conductivity as arising from perfect-crystal phonons that undergo scattering by other phonons, isotopes, defects, grain boundaries and pores. Where τ_{ph}, τ_{anh}^{-1}, τ_{iso}^{-1}, τ_{def}^{-1}, τ_{gb}^{-1} and $\tau_{\mathrm{pore}}^{-1}$ represent the total phonon relaxation time, anharmonic phonon-scattering, phonon-isotope scattering, phonon-defect scattering, phonon-grain boundary scattering and phonon-pore scattering, respectively. Details of the calculation formula of lattice thermal conductivity and the equation of corresponding relaxation times are given in the ESM. The contribution of porosity is plotted in Fig. 5(b), the nanoporosity can lead to the enhanced phonon scattering at the surfaces of pores as well as the thermal radiation within pores [34]. Fine porosity from 0% to 7.7% can not only significantly suppress the lattice thermal conductivity by about 11%, but also maintain the stability of material structure. Moreover, as the porosity caused by the difference of dendritic branch structure increases in turn, it is accompanied by the obvious change of grain size and grain boundary after sintering. The mechanism of grain boundaries (GB) and point defects (PD) should also be considered, Figs. 4(c) and 4(d) shows the contribution of each mechanism.

In addition, compared with the dense packing arrangement of octahedron morphology, the reduction of entirety thermal conductivity is huge from 4.6 W·m^{-1}·K^{-1} for 5# sample to 3.18 W·m^{-1}·K^{-1} for 4# sample at room temperature. In general, in the low temperature region the thermal conductivity mainly depends on the scattering mechanism of long wavelength phonons [35, 36], which mainly stem from grain boundaries and nanoprecipitates [37]. According to reported theoretical calculation work [38] that 70% of the κ_{lat} at 300 K is contributed by the mean free path shorter than 10 nm phonons. While the samples show grain boundary with a size greater than 1 μm after sintering, the contribution of GB is very trivial, which is consistent with theory calculation depicted in Figs. 4(d) and 4(e). Hence, the main reason for low κ maybe the existence of nanoprecipitates. The sintered matrix of 4# sample was tested by TEM, structures similar to nanoprecipitates in several different areas were observed in Fig. 3(c). The HRTEM image (Fig. 3(d)) shows significantly different lattice fringes of 0.291 nm which is consistent with $PbBr_2$ nanocrystals (*Pnam*). The electron diffraction pattern (Fig. 3(e)) transformed by FFT shows the same result. Figure 3(e) shows the corresponding diffraction patterns of $PbBr_2$ nanoprecipitates along [311] zone axis. These nano precipitates with sizes between 5 and 10 nm are capable of scattering phonons of different frequency [39, 40], which can cover most of the frequency range where phonons make a major contribution to thermal conductivity.

At the same time, because the octahedron sample has less defects, while the dendritic structure has many lattice distortions (Fig. 1(d)) caused in the synthesis and the overlapping and interlacing stacking structure of the dendritic branches can also contain lattice distortion (Fig. 3(f)). These lattice defects can scatter short-wave and medium-wave phonons [35, 41, 42], effectively enhancing the scattering of phonon transmission processes, which also explains why the thermal conductivity of dendritic structures is much lower than that of octahedron-derived sample. The calculated lattice thermal conductivities (κ_{lat}) of these samples are compared to the experimentally measured data in Fig. 5(f). Finally, the dendritic PbS sample (4#) showed the lowest thermal conductivity under the synergistic mechanism of several scatterings. The way in which these multiple scattering mechanisms act is shown schematically in Fig. 6(a).

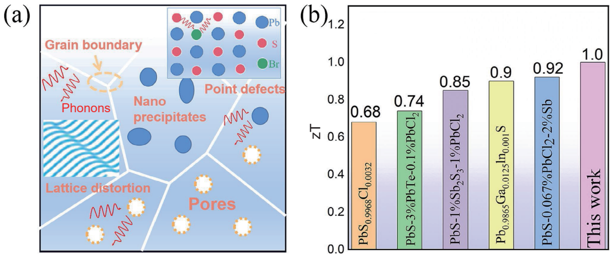

Figure 6 (a) Schematic illustration of the effect of multiscale defects on phonons, including grain boundary, point defects, lattice distortion, nano precipitates and pores. (b) The zT comparison of our 4# sample with previously reported PbS samples [10, 13, 16, 43, 44], all values were measured at 773 K.

The temperature dependence of zT comparison is shown in Fig. 5(f). Owing to low thermal conductivity and high-power factor, the 4# dendrite PbS sample shows a peak zT of 1.0 at 773 K. Compared with the existing literatures in Fig. 6(b), we find that the strategy by building porous structure has strong advantages. Moreover, the hydrothermal method avoids the pollution of toxic high vapor pressure of Pb and S [45].

4 Conclusion

PbS nanocrystals with branch structure are synthesized by solvent method. Compared with the dense packing of octahedral PbS, dendrite PbS with controlled morphonology can realize the formation of porous structure of bulk matrix. The obtained PbS monolith with porous structure has incomparable advantages of decreasing relative density and reducing its thermal conductivity, subsequently resulting excellent zT of 1.0 at 773 K. Theoretical calculation reveals that the enhanced scattering of phonons by the porous structure leads to low thermal conductivity. When the melting and alloying are the commonly used methods to construct thermoelectric devices, reemphasizing the importance of regulation by solution synthesis has certain guiding significance. Our finding revealed that bottom-up solution synthesis is an effective mean to prepare final matrix with porous structure, which can simultaneously enhance thermoelectric performance and improve portability of the thermoelectric device.

Acknowledgements

B.X. thanks financial supports from the National Natural Science Foundation of China (No. 21801133), Jiangsu Specially Appointed Professorship, Innovation and Entrepreneurship Talents in Jiangsu Province and State Key Laboratory of Coordination Chemistry, School of Chemistry and Chemical Engineering, Nanjing University. J. T. and T. F. acknowledge the support from the University of Utah.

Electronic Supplementary Material: Supplementary material (EDS, XRD patterns, SEM image, TG analysis and computational details with correlative experimental data diagram) is available in the online version of this article at https://doi.org/10.1007/s12274-022-4117-9.

References

[1] Zhao, D. L.; Tan, G. A review of thermoelectric cooling: Materials, modeling and applications. *Appl. Therm. Eng.* **2014**, *66*, 15–24.

[2] Shi, X. L.; Zou, J.; Chen, Z. G. Advanced thermoelectric design: From materials and structures to devices. *Chem. Rev.* **2020**, *120*, 7399–7515.

[3] He, W.; Zhang, G.; Zhang, X. X.; Ji, J.; Li, G. Q.; Zhao, X. D. Recent development and application of thermoelectric generator and cooler. *Appl. Energy* **2015**, *143*, 1–25.

[4] Fitriani; Ovik, R.; Long, B. D.; Barma, M. C.; Riaz, M.; Sabri, M. F. M.; Said, S. M.; Saidur, R. A review on nanostructures of high-temperature thermoelectric materials for waste heat recovery. *Renew. Sustain. Energy Rev.* **2016**, *64*, 635–659.

[5] Zhang, M. L.; Wang, Y. G.; Chen, W. X.; Dong, J. C.; Zheng, L. R.; Luo, J.; Wan, J. W.; Tian, S. B.; Cheong, W. C.; Wang, D. S. et al. Metal (hydr)oxides@polymer core-shell strategy to metal single-atom materials. *J. Am. Chem. Soc.* **2017**, *139*, 10976–10979.

[6] Liu, X. W.; Wang, D. S.; Li, Y. D. Synthesis and catalytic properties of bimetallic nanomaterials with various architectures. *Nano Today* **2012**, *7*, 448–466.

[7] Xu, B.; Feng, T. L.; Li, Z.; Zheng, W.; Wu, Y. Large-scale, solution-synthesized nanostructured composites for thermoelectric applications. *Adv. Mater.* **2018**, *30*, 1801904.

[8] Xu, B.; Feng, T. L.; Agne, M. T.; Zhou, L.; Ruan, X. L.; Snyder, G. J.; Wu, Y. Highly porous thermoelectric nanocomposites with low thermal conductivity and high figure of merit from large-scale solution-synthesized $Bi_2Te_{2.5}Se_{0.5}$ hollow nanostructures. *Angew. Chem., Int. Ed.* **2017**, *56*, 3546–3551.

[9] Parker, D.; Singh, D. J. High temperature thermoelectric properties of rock-salt structure PbS. *Solid State Commun.* **2014**, *182*, 34–37.

[10] Zhao, L. D.; Lo, S. H.; He, J. Q.; Li, H.; Biswas, K.; Androulakis, J.; Wu, C. I.; Hogan, T. P.; Chung, D. Y.; Dravid, V. P. et al. High performance thermoelectrics from earth-abundant materials: Enhanced figure of merit in PbS by second phase nanostructures. *J. Am. Chem. Soc.* **2011**, *133*, 20476–20487.

[11] Zhao, L. D.; He, J. Q.; Wu, C. I.; Hogan, T. P.; Zhou, X. Y.; Uher, C.; Dravid, V. P.; Kanatzidis, M. G. Thermoelectrics with earth abundant elements: High performance p-type PbS nanostructured with SrS and CaS. *J. Am. Chem. Soc.* **2012**, *134*, 7902–7912.

[12] Zhao, L. D.; He, J. Q.; Hao, S. Q.; Wu, C. I.; Hogan, T. P.; Wolverton, C.; Dravid, V. P.; Kanatzidis, M. G. Raising the thermoelectric performance of p-type PbS with endotaxial nanostructuring and valence-band offset engineering using CdS and ZnS. *J. Am. Chem. Soc.* **2012**, *134*, 16327–16336.

[13] Yang, J.; Zhang, X. Z.; Liu, G. W.; Zhao, L. J.; Liu, J. L.; Shi, Z. Q.; Ding, J. N.; Qiao, G. J. Multiscale structure and band configuration tuning to achieve high thermoelectric properties in n-type PbS bulks. *Nano Energy* **2020**, *74*, 104826.

[14] Wang, H.; Wang, J. L.; Cao, X. L.; Snyder, G. J. Thermoelectric alloys between PbSe and PbS with effective thermal conductivity reduction and high figure of merit. *J. Mater. Chem. A* **2014**, *2*, 3169–3174.

[15] Wang, J. L.; Wang, H.; Snyder, G. J.; Zhang, X.; Ni, Z. H.; Chen, Y. F. Characteristics of lattice thermal conductivity and carrier mobility of undoped PbSe-PbS solid solutions. *J. Phys. D Appl. Phys.* **2013**, *46*, 405301.

[16] Johnsen, S.; He, J. Q.; Androulakis, J.; Dravid, V. P.; Todorov, I.;

Chung, D. Y.; Kanatzidis, M. G. Nanostructures boost the thermoelectric performance of PbS. *J. Am. Chem. Soc.* **2011**, *133*, 3460–3470.

[17] Xiao, Y.; Wang, D. Y.; Zhang, Y.; Chen, C. R.; Zhang, S. X.; Wang, K. D.; Wang, G. T.; Pennycook, S. J.; Snyder, G. J.; Wu, H. J. et al. Band sharpening and band alignment enable high quality factor to enhance thermoelectric performance in *n*-type PbS. *J. Am. Chem. Soc.* **2020**, *142*, 4051–4060.

[18] Wu, Y. E.; Wang, D. S.; Li, Y. D. Understanding of the major reactions in solution synthesis of functional nanomaterials. *Sci. China Mater.* **2016**, *59*, 938–996.

[19] Wang, D. S.; Xie, T.; Li, Y. D. Nanocrystals: Solution-based synthesis and applications as nanocatalysts. *Nano Res.* **2009**, *2*, 30–46.

[20] Mourdikoudis, S.; Liz-Marzán, L. M. Oleylamine in nanoparticle synthesis. *Chem. Mater.* **2013**, *25*, 1465–1476.

[21] Wang, D. S.; Li, Y. D. Bimetallic nanocrystals: Liquid-phase synthesis and catalytic applications. *Adv. Mater.* **2011**, *23*, 1044–1060.

[22] Duan, H. H.; Wang, D. S.; Li, Y. D. Green chemistry for nanoparticle synthesis. *Chem. Soc. Rev.* **2015**, *44*, 5778–5792.

[23] Kuang, D.; Xu, A.; Fang, Y.; Liu, H.; Frommen, C.; Fenske, D. Surfactant-assisted growth of novel PbS dendritic nanostructures via facile hydrothermal process. *Adv. Mater.* **2003**, *15*, 1747–1750.

[24] Xia, Y. N.; Xiong, Y. J.; Lim, B.; Skrabalak, S. E. Shape-controlled synthesis of metal nanocrystals: Simple chemistry meets complex physics? *Angew. Chem., Int. Ed.* **2008**, *48*, 60–103.

[25] Pan, L.; Mitra, S.; Zhao, L. D.; Shen, Y. W.; Wang, Y. F.; Felser, C.; Berardan, D. The role of ionized impurity scattering on the thermoelectric performances of rock salt $AgPb_mSnSe_{2+m}$. *Adv. Funct. Mater.* **2016**, *26*, 5149–5157.

[26] Shuai, J.; Mao, J.; Song, S. W.; Zhu, Q.; Sun, J. F.; Wang, Y. M.; He, R.; Zhou, J. W.; Chen, G.; Singh, D. J. et al. Tuning the carrier scattering mechanism to effectively improve the thermoelectric properties. *Energy Environ. Sci.* **2017**, *10*, 799–807.

[27] Shi, X. L.; Wu, A. Y.; Feng, T. L.; Zheng, K.; Liu, W. D.; Sun, Q.; Hong, M.; Pantelides, S. T.; Chen, Z. G.; Zou, J. High thermoelectric performance in p-type polycrystalline Cd-doped SnSe achieved by a combination of cation vacancies and localized lattice engineering. *Adv. Energy Mater.* **2019**, *9*, 1803242.

[28] Nassary, M. M. The electrical conduction mechanisms and thermoelectric power of SnSe single crystals. *Turkish J. Phys.* **2009**, *33*, 201–208.

[29] Li, Y. W.; Li, F.; Dong, J. F.; Ge, Z. H.; Kang, F. Y.; He, J. Q.; Du, H. D.; Li, B.; Li, J. F. Enhanced mid-temperature thermoelectric performance of textured SnSe polycrystals made of solvothermally synthesized powders. *J. Mater. Chem. C* **2016**, *4*, 2047–2055.

[30] Fu, C. G.; Bai, S. Q.; Liu, Y. T.; Tang, Y. S.; Chen, L. D.; Zhao, X. B.; Zhu, T. J. Realizing high figure of merit in heavy-band p-type half-Heusler thermoelectric materials. *Nat. Commun.* **2015**, *6*, 8144.

[31] Li, J.; Zhang, X. Y.; Lin, S. Q.; Chen, Z. W.; Pei, Y. Z. Realizing the high thermoelectric performance of GeTe by Sb-doping and Se-alloying. *Chem. Mater.* **2017**, *29*, 605–611.

[32] Li, Y. H.; Wu, Z. H.; Lin, J. H.; Wang, Y. Y.; Mao, J. H.; Xie, H. Q.; Li, Z. Enhanced thermoelectric performance of hot-press Bi-doped n-type polycrystalline PbS. *Mater. Sci. Semicond. Process.* **2021**, *121*, 105393.

[33] Du, X. L.; Wang, Y. L.; Shi, R. N.; Mao, Z. Y.; Yuan, Z. H. Effects of anion and cation doping on the thermoelectric properties of n-type PbS. *J. Eur. Ceram. Soc.* **2018**, *38*, 3512–3517.

[34] Guo, F. K.; Cui, B.; Li, C.; Wang, Y. M.; Cao, J.; Zhang, X. H.; Ren, Z. F.; Cai, W.; Sui, J. H. Ultrahigh thermoelectric performance in environmentally friendly SnTe achieved through stress-induced lotus-seedpod-like grain boundaries. *Adv. Funct. Mater.* **2021**, *31*, 2101554.

[35] Aketo, D.; Shiga, T.; Shiomi, J. Scaling laws of cumulative thermal conductivity for short and long phonon mean free paths. *Appl. Phys. Lett.* **2014**, *105*, 131901.

[36] Wu, H. J.; Carrete, J.; Zhang, Z. Y.; Qu, Y. Q.; Shen, X. T.; Wang, Z.; Zhao, L. D.; He, J. Q. Strong enhancement of phonon scattering through nanoscale grains in lead sulfide thermoelectrics. *NPG Asia Mater.* **2014**, *6*, e108.

[37] Yang, X. L.; Carrete, J.; Wang, Z. Optimizing phonon scattering by nanoprecipitates in lead chalcogenides. *Appl. Phys. Lett.* **2016**, *108*, 113901.

[38] Xu, B.; Feng, T. L.; Li, Z.; Pantelides, S. T.; Wu, Y. Constructing highly porous thermoelectric monoliths with high-performance and improved portability from solution-synthesized shape-controlled nanocrystals. *Nano Lett.* **2018**, *18*, 4034–4039.

[39] Biswas, K.; He, J. Q.; Blum, I. D.; Wu, C. I.; Hogan, T. P.; Seidman, D. N.; Dravid, V. P.; Kanatzidis, M. G. High-performance bulk thermoelectrics with all-scale hierarchical architectures. *Nature* **2012**, *489*, 414–418.

[40] Zhang, H.; Hua, C. Y.; Ding, D.; Minnich, A. J. Length dependent thermal conductivity measurements yield phonon mean free path spectra in nanostructures. *Sci. Rep.* **2015**, *5*, 9121.

[41] Jiang, B. B.; Liu, X. X.; Wang, Q.; Cui, J.; Jia, B. H.; Zhu, Y. K.; Feng, J. H.; Qiu, Y.; Gu, M.; Ge, Z. et al. Realizing high-efficiency power generation in low-cost PbS-based thermoelectric materials. *Energy Environ. Sci.* **2020**, *13*, 579–591.

[42] Fu, L. W.; Yin, M. J.; Wu, D.; Li, W.; Feng, D.; Huang, L.; He, J. Q. Large enhancement of thermoelectric properties in n-type PbTe via dual-site point defects. *Energy Environ. Sci.* **2017**, *10*, 2030–2040.

[43] Wang, H.; Schechtel, E.; Pei, Y. Z.; Snyder, G. J. High thermoelectric efficiency of n-type PbS. *Adv. Energy Mater.* **2013**, *3*, 488–495.

[44] Luo, Z. Z.; Hao, S. Q.; Cai, S. T.; Bailey, T. P.; Tan, G. J.; Luo, Y. B.; Spanopoulos, I.; Uher, C.; Wolverton, C.; Dravid, V. P. et al. Enhancement of thermoelectric performance for n-type PbS through synergy of gap state and fermi level pinning. *J. Am. Chem. Soc.* **2019**, *141*, 6403–6412.

[45] Du, X. L.; Shi, R. N.; Guo, Y.; Wang, Y. L.; Ma, Y. C.; Yuan, Z. H. Enhanced thermoelectric properties of $Pb_{1-x}Bi_xS$ prepared with hydrothermal synthesis and microwave sintering. *Dalton Trans.* **2017**, *46*, 2129–2136.

Electronic Supplementary Material

High thermoelectric properties with low thermal conductivity due to the porous structure induced by the dendritic branching in n-type PbS

Zhenyu Zhu[1], Janak Tiwari [2], Tianli Feng[2], Zhan Shi[3], Yue Lou[1] (✉), and Biao Xu[1,4] (✉)

1 School of Chemistry and Chemical Engineering, Nanjing University of Science and Technology, Nanjing 210094, China
2 Department of Mechanical Engineering, The University of Utah, Salt Lake City, UT 84112, USA
3 State Key Laboratory of Inorganic Synthesis and Preparative Chemistry, College of Chemistry, Jilin University, Changchun 130012, China
4 State Key Laboratory of Coordination Chemistry, School of Chemistry and Chemical Engineering, Nanjing University, Nanjing 210000, China

Supporting information to https://doi.org/10.1007/s12274-022-4117-9

1.Characterization Results

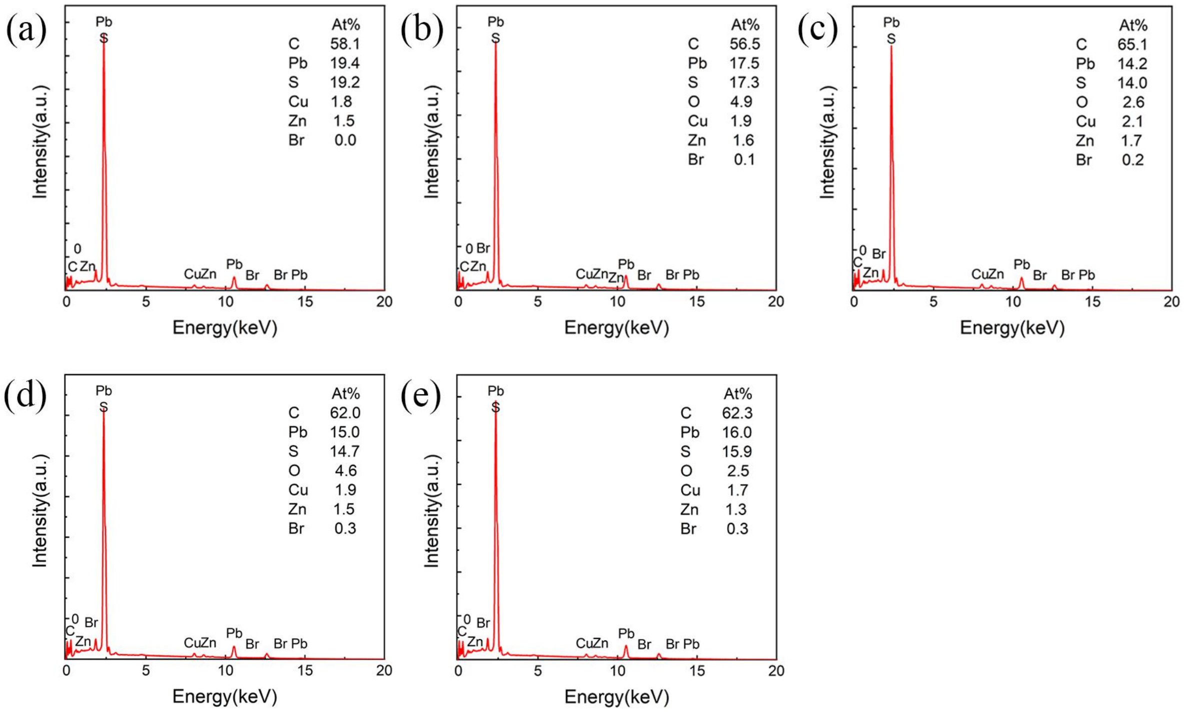

Figure S1 (a-e) The EDS of samples 1#, 2#, 3#, 4# and 5# respectively. The calculated elemental ratios are shown in Table S1.

Address correspondence to Yue Lou, wuxiaoshuai365@163.com; Biao Xu, xubiao@njust.edu.cn

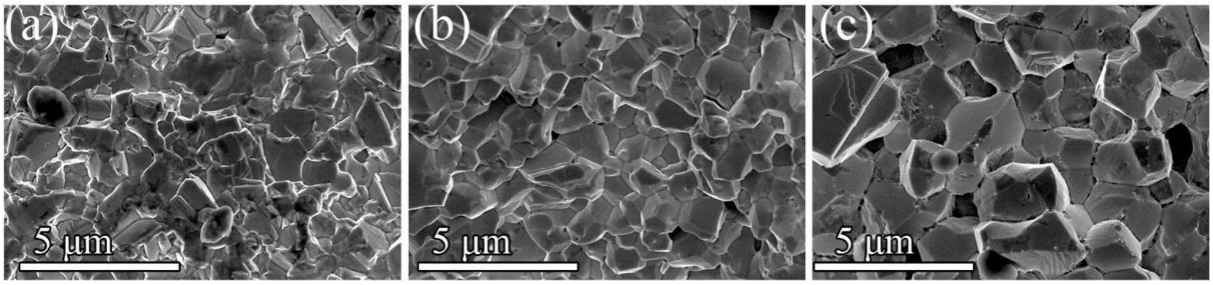

Figure S2 (a-c) The SEM image of the fractured surfaces of samples1#, 2# and 3# respectively.

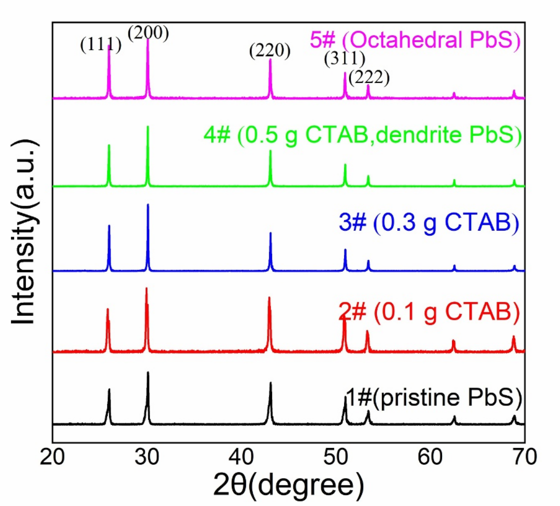

Figure S3 The XRD patterns of the sintered samples.

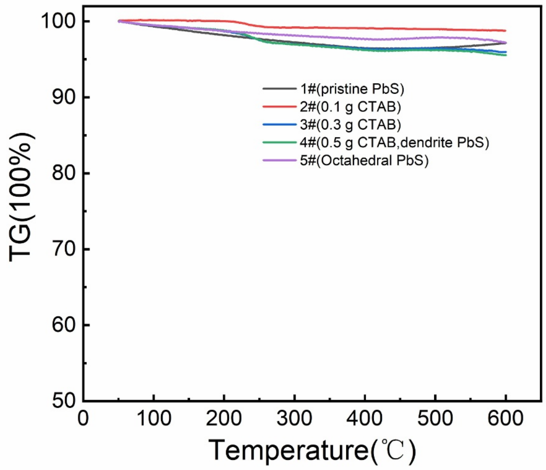

Figure S4 TG analysis of all samples, implying that all samples were stable between room temperature and 600 ℃.

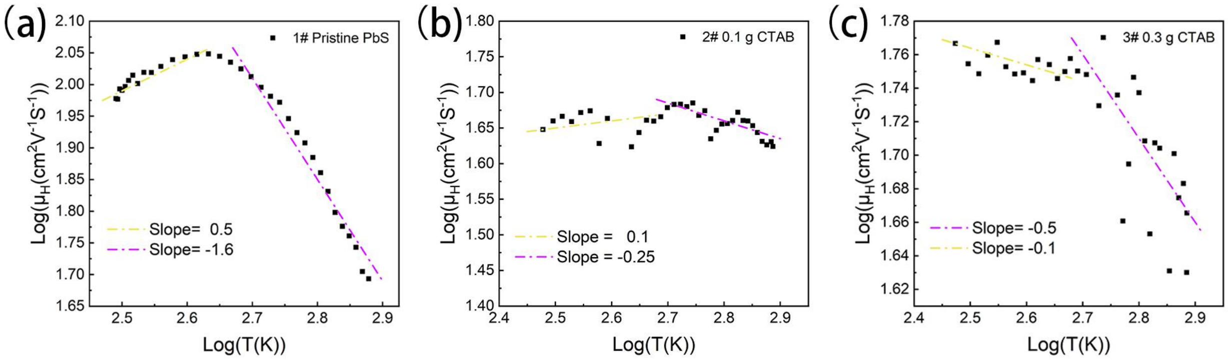

Figure S5 Temperature dependence of Carrier mobility μ_H: (a) 1# Pristine PbS, (b) 2# 0.1 g CTAB, (C) 3# 0.3 g CTAB.

2. Theory calculation Details

2.1 Details of the calculation formula of lattice thermal conductivity

$$\boldsymbol{\kappa_{lat}} = \frac{\mathbf{1}}{\boldsymbol{NV_{cell}}}(\mathbf{1}-\boldsymbol{P})\sum_{j}^{6}\sum_{q}\frac{\boldsymbol{h^2\omega^2(q,j)}}{\boldsymbol{k_BT^2}}\frac{\boldsymbol{e^{h\omega(q,j)/k_BT}}}{\left(\boldsymbol{e^{h\omega(q,j)/k_BT}}-\mathbf{1}\right)^2}\boldsymbol{\upsilon_{ph,x}}^2\boldsymbol{(q,j)\tau_{ph}(q,j)}\#\mathbf{Eq.\,1}$$

In this formula, *h* represents the Plank constant, k_B represents the Boltzmann constant, T is temperature in Kelvin, ω(q, j) is the perfect crystal phonon angular frequency, q is the phonon wavevector, *j* is the phonon branch, $V_{ph,x}$ is the phonon group velocity component in direction *x*, *N* is the number of q points sampled uniformly throughout the first Brillouin zone, and V_{cell} is the volume of a primitive unit cell. The summation is taken over all the phonon modes (q, j). The effect of nano pores is studied beyond the effective medium approximation by considering the phonon-pore scattering. P is the porosity and the factor (1- P) considers the loss of material.

2.2 The equation of corresponding relaxation times

The isotope, defect, and grain boundary scattering rates[1-4] are calculated by

$$\frac{\mathbf{1}}{\boldsymbol{\tau_{iso}(q,j)}} = \frac{\boldsymbol{\pi}}{\mathbf{2}}\boldsymbol{g_{iso}\omega^2(q,j)DOS(\omega)}\#\mathbf{Eq.\,2}$$

$$\frac{\mathbf{1}}{\boldsymbol{\tau_{def}(q,j)}} = \frac{\boldsymbol{\pi}}{\mathbf{2}}\boldsymbol{g_{def}\omega^2(q,j)DOS(\omega)}\#\mathbf{Eq.\,3}$$

$$\frac{\mathbf{1}}{\boldsymbol{\tau_{gb}(q,j)}} = \frac{\boldsymbol{\upsilon_{ph}(q,j)}}{\boldsymbol{D_{grain}}}\#\mathbf{Eq.\,4}$$

Where g_{iso} and g_{def} are the mass disorders induced by the natural Pb/S isotopes and the Br defects in the samples given by $g = \eta(\frac{\Delta M}{M})^2$, where η is the concentration of isotopes (defects), and ΔM is the mass difference between isotopes (defects) and the pristine Pb/S atoms. *DOS(ω)* is the normalized density of states of the pristine PbS. D_{grain} is the average grain diameter.

The phonon-pore scattering[5] is determined by

$$\frac{\mathbf{1}}{\boldsymbol{\tau_{pore}(q,j)}} = \frac{\boldsymbol{P}}{\mathbf{2}}\frac{\mathbf{1}}{\boldsymbol{\tau_{bulk}(q,j)}}\frac{\boldsymbol{3P\upsilon_{ph}(q,j)}}{\boldsymbol{2D_{pore}}}\#\mathbf{Eq.\,5}$$

where D_{pore} is the average pore diameter.

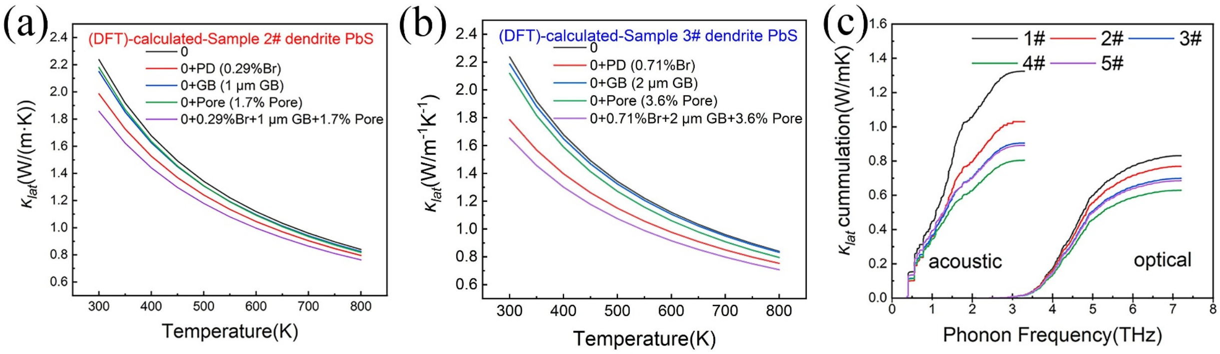

Figure S6 (a) DFT-calculated κ_{lat} of 2# by considering the phonon scattering mechanisms of PD, GB and Pore. (b) DFT-calculated κ_{lat} of 3# by considering the phonon scattering mechanisms of PD, GB and Pore. (c) The lattice thermal conductivity accumulations as a function of phonon frequency for acoustic and optical phonons.

Table S1 The data used in the thermal conductivity calculation

Sample No.	Relative density	Br doping concentration (atom %)	Grain size (μm)	Average grain Size (μm)	Porosity	Pore diameter(μm)
1#	99.6%	0.4		1	0	0
2#	98.3%	0.29	0.5-1	1	1.7%	0.39
3#	96.4%	0.71	1.5-2	2	3.6%	0.8
4#	92.3%	1.00	2-3	2.5	7.7%	0.55
5#	98.1%	1.00	6-7	6.5	1.9%	0.5

Reference

[1] Feng T, Ruan X. Prediction of Spectral Phonon Mean Free Path and Thermal Conductivity with Applications to Thermoelectrics and Thermal Management: A Review[J]. *J. Nanomater*. 2014, 2014: 1-25.

[2] Feng T, Qiu B, Ruan X. Coupling between phonon-phonon and phonon-impurity scattering: A critical revisit of the spectral Matthiessen's rule[J]. *Phys. Rev. B.* 2015, 92(23).

[3] Tamura S-I. Isotope scattering of dispersive phonons in Ge[J]. *Phys. Rev. B.* 1983, 27(2): 858-866.

[4] Garg J, Bonini N, Kozinsky B, et al. Role of disorder and anharmonicity in the thermal conductivity of silicon-germanium alloys: a first-principles study[J]. *Phys Rev Lett*, 2011, 106(4): 045901.

[5] Dettori R, Melis C, Cartoixà X, et al. Model for thermal conductivity in nanoporous silicon from atomistic simulations[J]. *Phys. Rev. B.* 2015, 91(5).